Protein turnover dynamics suggest a diffusion-to-capture mechanism for peri-basal body recruitment and retention of intraflagellar transport proteins

Jaime V. K. Hibbard[a], Neftali Vazquez[a], Rohit Satija[b], and John B. Wallingford[a,*]
[a]Department of Molecular Biosciences, University of Texas at Austin, Austin, TX 78712; [b]California Institute of Quantitative Biosciences, University of California, Berkeley, Berkeley, CA 94720

ABSTRACT **Intraflagellar transport (IFT) is essential for construction and maintenance of cilia. IFT proteins concentrate at the basal body where they are thought to assemble into trains and bind cargoes for transport. To study the mechanisms of IFT recruitment to this peri-basal body pool, we quantified protein dynamics of eight IFT proteins, as well as five other basal body localizing proteins using fluorescence recovery after photobleaching in vertebrate multiciliated cells. We found that members of the IFT-A and IFT-B protein complexes show distinct turnover kinetics from other basal body components. Additionally, known IFT subcomplexes displayed shared dynamics, suggesting shared basal body recruitment and/or retention mechanisms. Finally, we evaluated the mechanisms of basal body recruitment by depolymerizing cytosolic MTs, which suggested that IFT proteins are recruited to basal bodies through a diffusion-to-capture mechanism. Our survey of IFT protein dynamics provides new insights into IFT recruitment to basal bodies, a crucial step in ciliogenesis and ciliary signaling.**

Monitoring Editor
Wallace Marshall
University of California, San Francisco

Received: Nov 16, 2020
Revised: Mar 15, 2021
Accepted: Mar 30, 2021

INTRODUCTION

Construction and maintenance of cilia require the movement of protein cargoes by a conserved active transport process termed intraflagellar transport (IFT) (Kozminski *et al.*, 1993; Sung and Leroux, 2013; Lechtreck, 2015). IFT proteins act as adaptors between cargoes and the microtubule (MT) motors kinesin and dynein. Kinesin-II drives anterograde IFT, carrying cargoes from the cell body to cilium tip (Walther *et al.*, 1994; Kozminski *et al.*, 1995; Cole *et al.*, 1998). Retrograde IFT is powered by IFT dynein and recycles signaling molecules and other proteins from the ciliary tip to the basal body at the base of cilia (Pazour *et al.*, 1998, 1999; Porter *et al.*, 1999; Signor *et al.*, 1999).

While IFT proteins have an essential axonemal function, the highest concentration of IFT proteins in the cell is found in a pool surrounding the basal body (Vashishtha *et al.*, 1996; Cole *et al.*, 1998; Deane *et al.*, 2001; Jurczyk *et al.*, 2004; Qin *et al.*, 2004;Lechtreck, 2015). This peri-basal body pool is proposed to be the site of IFT cargo loading (Lechtreck, 2015), which is practical considering that the higher local concentration of ciliary proteins within this pool can facilitate faster reaction kinetics. Additionally, perturbations that deplete the peri-basal body IFT pool are associated with loss of cilia (Jurczyk *et al.*, 2004; Richey and Qin, 2012; Čajánek and Nigg, 2014; Toriyama *et al.*, 2016), implicating the peri-basal body pool of IFT in the broad class of human diseases termed ciliopathies (Hildebrandt *et al.*, 2011). Despite its importance for vertebrate development, the mechanisms by which IFT proteins are recruited to the peri-basal body pool from the cytoplasm remain unclear.

Multiple hypotheses could explain IFT protein localization to basal bodies. For example, IFT proteins might be actively transported to the basal body along cytosolic MTs (Mukhopadhyay *et al.*, 2010; Hao *et al.*, 2011; Fu *et al.*, 2016). This hypothesis is enticing because the basal body serves as the MT organizing center for not only ciliary but also cytosolic MTs (Tucker, 1984; LeDizet and Piperno, 1986; Sandoz *et al.*, 1988). Indeed, ciliary protein Ccdc66 and ciliary receptor Rhodopsin are transported along cytoplasmic MTs via dynein motors

This article was published online ahead of print in MBoC in Press (http://www.molbiolcell.org/cgi/doi/10.1091/mbc.E20-11-0717) on April 7, 2021.

*Address correspondence to: John B. Wallingford (Wallingford@austin.utexas.edu).

Abbreviations used: FRAP, fluorescence recovery after photobleaching; IFT, intraflagellar transport; KD, knockdown; MCC, multiciliated cell; MMR, Marc's modified Ringer's; MO, morpholino oligonucleotide; MT, microtubule; ROI, region of interest.

(Tai *et al.*, 1999; Conkar *et al.*, 2019; Prosser and Pelletier, 2020). An alternative "diffusion-to-capture" mechanism, whereby proteins freely diffuse until they find a docking site at their appropriate subcellular localization, plays an important role in localizing some ciliary proteins (Harris *et al.*, 2016). Disruption of substructures of the basal body known as distal appendages leads to loss of the peri-basal body IFT pool, so these structures may act as a capture site (Deane *et al.*, 2001; Singla *et al.*, 2010; Schmidt *et al.*, 2012; Čajánek and Nigg, 2014; Yang *et al.*, 2018).

Importantly, these mechanisms are not mutually exclusive, as the IFT proteins form complexes of multiple distinct subunits. These include two highly conserved protein complexes, IFT-A and IFT-B, composed of 6 and 16 proteins, respectively (Taschner and Lorentzen, 2016). IFT-A consists of both "core" and "peripheral" subunits, and IFT-B is known to consist of two subcomplexes, IFT-B1 and IFT-B2 (Piperno and Mead, 1997; Cole *et al.*, 1998; Lucker *et al.*, 2005; Lucker *et al.*, 2010; Mukhopadhyay *et al.*, 2010; Taschner *et al.*, 2011, 2016; Behal *et al.*, 2012; Katoh *et al.*, 2016). At the basal body, these subunits, along with IFT motors, assemble into higher-order structures called trains (Jordan *et al.*, 2018; Webb *et al.*, 2020). Whether subcomplexes share basal body recruitment and retention mechanisms remains unclear.

Recruitment and retention of IFT proteins near basal bodies are inherently dynamic processes, yet most results concerning the peri-basal body pool of IFT have been generated using static endpoint assays such as immunofluorescence. Recently, however, dynamic imaging has provided new insights into this important problem (Buisson *et al.*, 2013; Wingfield *et al.*, 2017; McInally *et al.*, 2019; Yang *et al.*, 2019). Notably, a recent study in *Chlamydomonas* has shown that the majority of the IFT peri-basal body pool is maintained via exhange with cytosolic IFT proteins (Wingfield *et al.*, 2017). Furthermore, that study found that certain IFT-B members have similar kinetics of turnover in the peri-basal body pool, consistent with the idea that IFT-B subcomplexes are preassembled in the cytoplasm before recuitment to the basal body (Wingfield *et al.*, 2017). However, a comprehensive survey of IFT protein dynamics at basal bodies has not been reported.

Finally, dynamic studies of the peri-basal body IFT pool have primarily been conducted in unicellular organisms such as *Chlamydomonas, Giardia,* and *Trypanosoma* (Buisson *et al.*, 2013; Wingfield *et al.*, 2017; McInally *et al.*, 2019; Yang *et al.*, 2019). Though many molecular mechanisms of ciliogenesis are shared between these organisms and vertebrates (Sung and Leroux, 2013; Sigg *et al.*, 2017), other mechanisms, such as the CPLANE complex, are not evolutionarily conserved (Adler and Wallingford, 2017). We therefore quantified protein dynamics of several components of IFT-A and IFT-B, as well as other ciliary proteins at the basal body pool using fluorescence recovery after photobleaching (FRAP) in vertebrate multiciliated cells (MCCs). We discovered that members of the IFT-A and IFT-B protein complexes show distinct turnover kinetics. These different kinetics suggest unique molecular mechanisms of IFT protein retention in the basal body pool, facilitated by different protein–protein interactions. Furthermore, we performed the first direct test of the hypothesis that cytosolic MTs could provide tracks for active transport of IFT proteins to basal bodies.

RESULTS AND DISCUSSION

Distinct turnover kinetics for ciliary proteins in the basal body pool

To quantify protein dynamics in vertebrate MCCs in vivo, we turned to the epidermis of *Xenopus laevis* embryos. This system has emerged in recent years as a key platform for in vivo analysis of IFT and other ciliary systems (Werner and Mitchell, 2012; Walentek and Quigley, 2017). We expressed fluorescently tagged ciliary proteins using methods described previously (Brooks and Wallingford, 2015) and used confocal microscopy to image the en face apical optical section of MCCs, which contains basal bodies, and performed FRAP (Figure 1A). We bleached small regions of interest (ROIs) containing three to five basal bodies within our field of view (Figure 1B) and used a neighboring cell with nonbleached basal bodies outside the ROI to correct for changes to background fluorescence during imaging. Under our experimental conditions, half-times were quite short (~20 s for most proteins tested) (Supplemental Figure S1), which is consistent with a freely diffusing protein. We therefore used mobile fraction to indicate the fraction of basal body protein that was exchanging with a cytosolic pool versus stable in the basal body pool. On short timescales (seconds to minutes), proteins that are stably associated with the basal body will be less able to exchange protein contents and will have a lower mobile fraction value (Axelrod *et al.*, 1976; Reits and Neefjes, 2001).

We first established baseline parameters by performing FRAP on a diverse group of known basal body-associated proteins (Figure 1G). As expected for structural components of the basal body, we found that BFP or GFP fusions to Centrin2, Ofd1, and Cep164 displayed very small mobile fraction values (Figure 1, B, D, and H), indicating that they are stably retained and exchange slowly with the cytoplasm (Paoletti *et al.*, 1996; Singla *et al.*, 2010; Schmidt *et al.*, 2012). By contrast, known ciliogenesis regulator Ttbk2 (Goetz *et al.*, 2012) displayed a much higher mobile fraction, suggesting it is not stably retained but rather exchanges more freely with the cytoplasm. Finally, Ccdc66 is implicated in the recruitment of ciliary proteins and displayed an intermediate FRAP profile (Conkar *et al.*, 2017, 2019;), far more dynamic than the structural components, but slower than Ttbk2. These data demonstrate the efficacy of our experimental platform for exploring protein dynamics and suggest that ciliary and centriolar proteins display diverse patterns of turnover at basal bodies in MCCs.

Functionally related IFT subcomplexes display shared protein dynamics

We next sought to use our FRAP platform to explore the dynamics of IFT protein retention in the peri-basal body pool. We chose eight IFT proteins (bold outlines in Figure 1C) for analysis to sample the dynamics of the full range of known IFT subcomplexes.

The first trend that was clear in our data was that known subcomplexes displayed shared dynamics. For example, the IFT-B complex is known to be composed of two subcomplexes, IFT-B1 and IFT-B2 (Taschner *et al.*, 2016). We examined the kinetics of recovery for three subunits of the IFT-B1 complex: Ift46, Ift52, and Ift81; all showed similar mean mobile fraction values (47, 47, and 43%, respectively). Strikingly, however, the IFT-B2 protein Ift20 displayed significantly different dynamics, with a mean mobile fraction value of 37% (Figure 1, E and H). The distinct turnover kinetics suggests the possibility that the IFT-B1 and IFT-B2 subcomplexes are retained in the peri-basal body pool by distinct mechanisms.

We also observed differences in the turnover dynamics of IFT-A proteins. First, all IFT-A components tested displayed significantly greater mobile fractions as compared with IFT-B (Figure 1H). IFT-A is comprised of biochemically distinct "core" and "peripheral" subunits (Mukhopadhyay *et al.*, 2010; Behal *et al.*, 2012; Zhu *et al.*, 2017). Two core (Ift122/Ift144) and one peripheral protein (Ift121) all displayed shared dynamics, each with a mean mobile fraction value of ~57% (Figure 1H). Finally, the peripheral IFT-A component Ift43 consistently displayed different turnover dynamics when compared

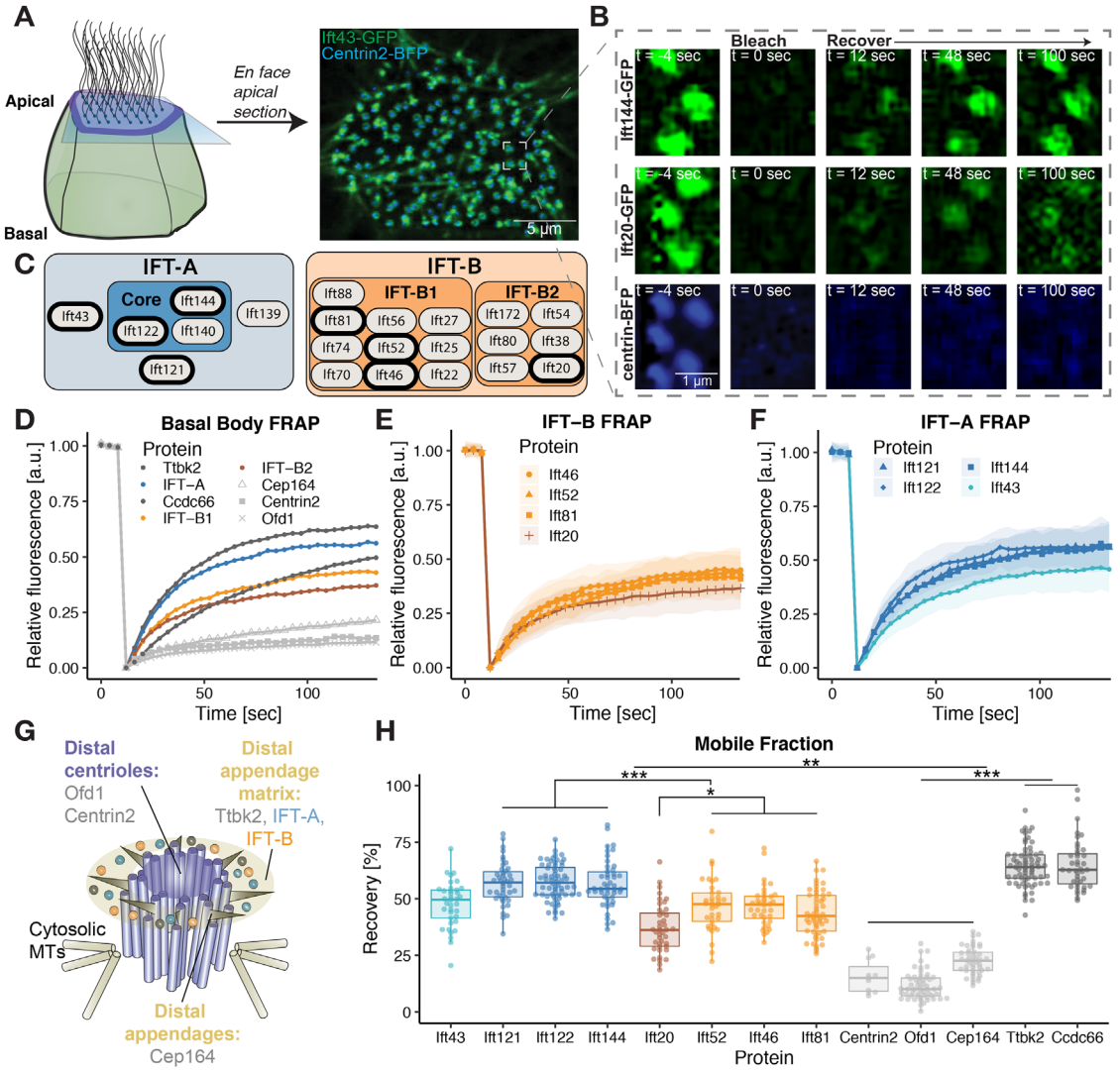

FIGURE 1: Functionally related proteins show distinct turnover kinetics in the basal body pool. (A) Schematic representation of FRAP experimental setup. IFT43-GFP accumulates around Centrin2-BFP, a marker for basal bodies. (B) Representative images from FRAP experiments of Ift144-GFP, Ift20-GFP, and Centrin2-BFP. (C) Schematic of IFT-A and IFT-B complexes. Proteins investigated in this report are bolded. (D) FRAP recovery curves of IFT-A proteins (averaged from Ift144-GFP, GFP-Ift122, and Ift121-GFP), IFT-B1 proteins (averaged from Ift81-GFP, Ift52-mNG, and Ift46-mNG), IFT-B2 protein Ift20-GFP, structural basal body components (Cep164-GFP, Centrin2-BFP, GFP-Ofd1), and basal body regulators (GFP-Ttbk2, GFP-Ccdc66). For clarity of presentation, error bars are removed. (E) FRAP recovery curves of IFT-B proteins. Shaded area corresponds to SD. (F) FRAP recovery curves of IFT-A proteins. Shaded area corresponds to SD. (G) Schematic representation of a basal body, showing the localization of different proteins. (H) Mobile fraction quantification of basal body turnover kinetics for investigated proteins. Several statistical differences are noted in the tree; for full discussion of differences, see Supplemental Table S2.

with the other IFT-A proteins (Figure 1, F and H). Importantly, this finding is consistent with multiple studies suggesting Ift43 is substoichiometric in the IFT-A complex (Mukhopadhyay *et al.*, 2010; Behal *et al.*, 2012).

These data in vertebrate MCCs confirm and extend previous findings from *Chlamydomonas* and trypanosomes (Buisson *et al.*, 2013; Wingfield *et al.*, 2017). The trends observed in IFT dynamics here, with IFT-A proteins being more dynamic than IFT-B and with IFT-B1 more dynamic than IFT-B2, are consistent with *Chlamydomonas* (Wingfield *et al.*, 2017). Additionally, the mobile fraction identified here for Ift52 (47%) is nearly identical to the 46% recovery observed for GFP::IFT52 in trypanosomes (Buisson *et al.*, 2013).

Finally, the turnover trends observed here, along with data from *Chlamydomonas*, establish shared basal body turnover dynamics within functionally related IFT subcomplexes as an evolutionarily conserved feature (Wingfield *et al.*, 2017). Moreover, these conserved turnover dynamics suggest that IFT protein complexes are likely retained at basal bodies as assembled subcomplexes, rather than as individual subunits. Coupled to biochemical findings that many individual IFT proteins are unstable without their binding partners (Richey and Qin, 2012; Bhogaraju *et al.*, 2013; Taschner *et al.*, 2014), our live imaging data suggest that IFT subcomplex assembly likely occurs in the cytoplasm, rather than in the basal body pool.

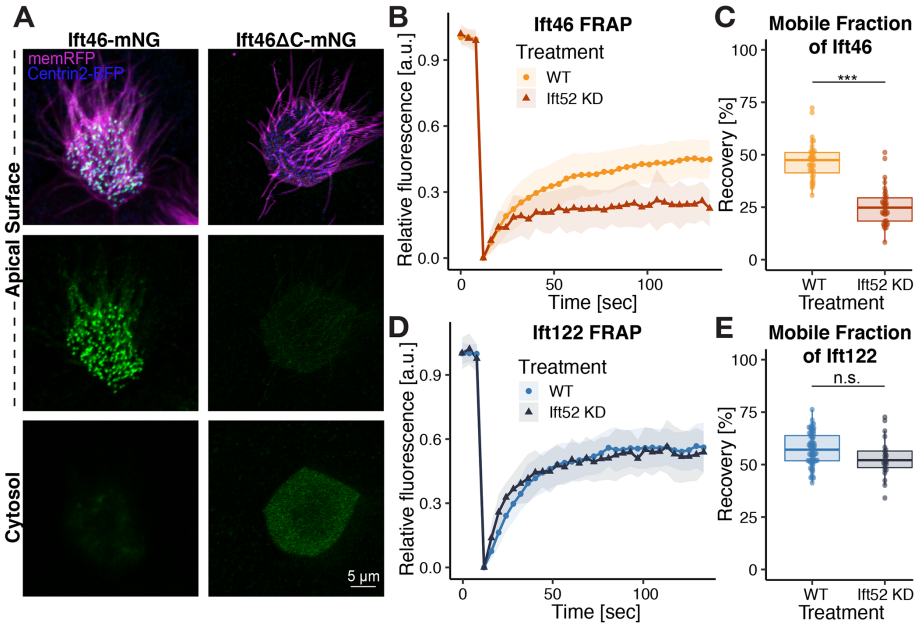

FIGURE 2: Ift52 is required for the recruitment and normal turnover of Ift46 at basal bodies. (A) Imaging of Ift46-mNG (left panel) and Ift46ΔC-mNG (right panel). (B) FRAP of Ift46-mNG in WT embryos compared with *ift52* KD. (C) The mobile fraction value of Ift46-mNG is significantly lower on KD of Ift52. (D) FRAP recovery of GFP-Ift122, an IFT-A protein, is not affected by *ift52* KD. (E) Mobile fraction quantification of GFP-Ift122 in WT and *ift52* KD embryos.

Intra-IFT protein interactions control IFT basal body turnover kinetics

To explore the significance of the observed pattern of IFT protein dynamics in the peri-basal body pool, we next asked if known protein–protein interactions within IFT complexes impact IFT protein turnover. We focused on Ift46, an IFT-B1 member, because it is known to be recruited to the basal body by its interaction with Ift52 in *Chlamydomonas* (Lv *et al.*, 2017). First, we confirmed that this functional interaction is conserved in *Xenopus* by expressing Ift46 that lacked its C-terminal Ift52 binding domain (Ift46ΔC-mNG). We observe that while full-length Ift46-mNG was properly recruited to the basal body, Ift46ΔC-mNG was not and instead displayed strong diffuse signal throughout the cytoplasm (Figure 2A). This result further validates the conservation of basal body recruitment mechanisms between *Chlamydomonas* and vertebrates.

As Ift46 recruitment to basal bodies is dependent on its interaction with Ift52 (Lv *et al.*, 2017), we hypothesized that the disruption of Ift52 would lead to changes in basal body turnover dynamics of Ift46, so we assessed FRAP turnover after knockdown (KD) of *ift52* with a previously described morpholino (Dammermann *et al.*, 2009; Drew *et al.*, 2017). KD of *ift52* leads to decreased levels of Ift46-mNG at basal bodies, as expected, and importantly, this phenotype could be rescued by re-expression of Ift52 (Supplemental Figure S2). Consistent with the hypothesis that Ift52 loss will disrupt the FRAP kinetics of its binding partner, we determined that Ift46 displayed significantly reduced turnover in the basal body pool on KD of *ift52* (Figure 2, B and C). As there is still remnant Ift46 enrichment at the basal body (Supplemental Figure S2), we hypothesize that *ift52* KD reduces the number of basal body binding spots available to Ift46, resulting in less dynamic turnover.

As a control for specificity, we noted that IFT-B is not required for IFT-A recruitment to basal bodies (Brown *et al.*, 2015), and we found that Ift122 dynamics were unaffected by *ift52* KD (Figure 2, D and E). These data validate the utility of our FRAP system to explore the mechanisms of IFT retention at basal bodies.

IFT recruitment kinetics at basal bodies are unaltered during cilia regeneration

The IFT retention kinetics described above were obtained in full-length cilia, which homeostatically maintain a relatively constant length. Interestingly, during cilia regeneration, several aspects of IFT are altered, as substantially more cargoes must be transported to build the growing axoneme. Indeed, flagellar regeneration in *Chlamydomonas* is characterized by changes in the size of the peri-basal body pool, IFT train size, and in cargo loading onto IFT trains (Engel *et al.*, 2009; Ludington *et al.*, 2013; Wren *et al.*, 2013; Craft *et al.*, 2015). On the one hand, ciliary growth requires the import of thousands of copies of ciliary precursors (Qin *et al.*, 2004), so we might expect to observe altered kinetics of IFT during regeneration. Alternatively, steady-state basal body turnover of IFT could be sufficient to "prime" cilia for regeneration. In this model, an increase in cargoes per IFT train could be sufficient to increase ciliary cargo import, without the need to change IFT recruitment to basal bodies. Consistent with this latter hypothesis, cargo-loading on IFT trains scales inversely with ciliary length (Engel *et al.*, 2009; Wren *et al.*, 2013; Craft *et al.*, 2015).

To ask if IFT turnover rates differ during ciliary growth, we used a previously described method for deciliation in *Xenopus* MCCs (Werner and Mitchell, 2013) and then quantified the timecourse of cilia regeneration using confocal imaging at 30-min intervals. *Xenopus* MCCs underwent an obvious lag phase before beginning regrowth, with no evident increase in cilia length in the first 60 min (Figure 3, A and B). Regeneration lag phases are variable across organisms, with protozoans displaying a ~20-min lag before regeneration (Rosenbaum and Child, 1967; Tamm, 1967) and no apparent lag phase in *Chlamydomonas* (Rosenbaum *et al.*, 1969). Cilia then grew at a fairly consistent rate over the next 2 h (Figure 3B).

We first examined basal body turnover of the IFT-A protein Ift121 immediately following deciliation and at early and mid-regrowth timepoints (Figure 3, C and D). Interestingly, we observed no change in the basal body turnover of Ift121 during cilia regeneration (Figure 3, C and D). These data suggest that retention of Ift121 at the basal body is not adjusted during ciliary regeneration. Based on our previous data, we expect other members of the IFT-A complex to share basal body recruitment mechanisms. We therefore expect steady-state turnover of IFT-A to be sufficient to prime cilia for regeneration. Alternatively, it is possible that while retention is unaltered during cilia regeneration there is a higher flux of IFT-A proteins to the basal body and into the axoneme.

We also observed the turnover of IFT-B protein Ift81 immediately following deciliation and at 1 h postdeciliation. Immediately following deciliation, there is little new growth of cilia (Figure 3, A and B). At this timepoint, we observed no significant difference between the mobile fraction of Ift81, compared with values obtained from embryos with full-length cilia (Figure 3, C and D). Interestingly, we note that there was a slight, but significant difference in the mobile fraction obtained from embryos at 1 h postdeciliation, where

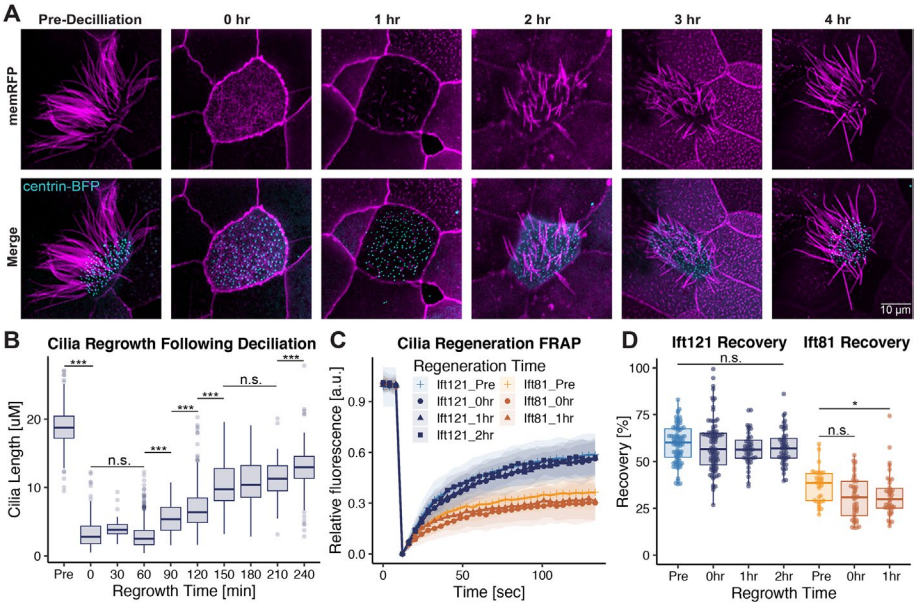

FIGURE 3: Induced cilia regeneration has no effect on IFT protein dynamics at the basal body. (A) Time course tracking cilia regrowth, predeciliation, postdeciliation and every hour up to the fourth hour timepoint. (B) Quantification of ciliary length prior to and during ciliary regeneration. (C) FRAP recovery curves of Ift121-GFP and Ift81-GFP at different timepoints pre-, post-, and during ciliary regeneration. (D) Mobile fraction values of Ift121-GFP and Ift81-GFP pre-, post-, and during ciliary regeneration.

regrowth is actively occuring (Figure 3, C and D) from cilia not undergoing regneration (Figure 3, C and D).

These data further address the relative contributions of exchange from cytoplasm and axonemal IFT trains to the observed basal body turnover dynamics. Immediately following deciliation, there is little or no contribution from returning IFT trains to the basal body pool. Nonetheless, basal body turnover dynamics remain constant, demonstrating that the basal body pool of IFT is maintained by exchange with the cytosolic pool, rather than recycling from the cilia. As cell body fractions have 10- to 50-fold higher abundance of IFT proteins than flagellar fractions, it fits that IFT proteins coming and leaving in trains make minor contributions to the basal body pool (Ahmed *et al.*, 2008). Finally, these findings are also consistent with data that suggest an "open" system for IFT-A, where IFT-A proteins returning from the axoneme following retrograde transport immediately re-enter the cytosolic pool (Wingfield *et al.*, 2017).

Cytosolic MTs are dispensable for IFT recruitment to basal bodies

Next, we sought to explore the mechanisms of IFT transport to basal bodies from the cytosol. To investigate the potential that IFT proteins are themselves a cargo for MT-based active transport to basal bodies, we developed a system to specifically depolymerize cytosolic MTs in *Xenopus* MCCs in vivo. Cold-shock techniques are known to depolymerize cytosolic MTs without affecting ciliary MTs (Behnke and Forer, 1967; Burton, 1968). However, cytosolic MTs quickly reform on return to room temperature. Because nocodazole inhibits MT polymerization (De Brabander *et al.*, 1976; Hoebeke *et al.*, 1976), we used a combination treatment of cold shock and nocodazole (CS+noc). Transverse sections of *Xenopus* MCCs (Figure 4, A and B) show this treatment effectively depolymerized cytosolic MTs (Figure 4C), without affecting ciliary MTs (Figure 4D).

To confirm this approach disrupted active transport to basal bodies, we examined the turnover kinetics of Ccdc66, which is known to require cytosolic MTs for its localization to the base of primary cilia (Conkar *et al.*, 2019). FRAP following CS+noc treatment of MCCs revealed a significant decrease in the mobile fraction value for Ccdc66, as compared with the untreated control (Figure 4E). The ~19% mobile fraction decrease is consistent with the ~15% decrease observed for centrosomal localization in RPE cells (Conkar *et al.*, 2019).

By contrast, all tested IFT proteins displayed no change after CS+noc treatment. FRAP recovery kinetics of IFT-A proteins Ift121, Ift122, and Ift144 appeared identical with and without CS+noc treatment (Figure 5A). Similarly, FRAP kinetics of IFT-B proteins Ift52 and Ift20 did not change with CS+noc treatment (Figure 5B). There was no statistically significant change in the mobile fraction values of any IFT protein after disruption of cytosolic MTs (Figure 5, C and D). These data demonstrate that cytosolic MTs are dispensable for normal retention of IFT proteins at basal bodies, suggesting that a diffusion-to-capture mechanism is responsible for maintenance of the IFT basal body pool. Consistent with this diffusion-to-capture mechanism, data from trypanosomes showed that temperature changes influenced the rate of basal body turnover of GFP::IFT52 (Buisson *et al.*, 2013). Increased temperature would be expected to increase the kinetic rates of diffusion and binding, so we would expect faster turnover, and this is exactly what was observed with GFP::IFT52 in trypanosomes (Buisson *et al.*, 2013).

In vivo quantification of IFT protein diffusion and binding kinetics by analysis and modeling of FRAP data

Elucidation of kinetic rate constants is essential for complete understanding of biological processes. To determine the kinetic rate constants of the diffusion-to-capture mechanism for IFT transport to basal bodies, we used a combination of curve fitting and modeling techniques.

When FRAP recovery is dominated by binding to a subcellular structure, FRAP curve-fitting allows for elucidation of binding kinetics (Sprague and McNally, 2005). Therefore, we first verified that our FRAP recoveries were within a binding-dominant regime. To do so, we changed the size of our bleaching and analysis region from 5 to 1 µm^2. If diffusion is a major contributor to FRAP recovery, smaller bleaching and analysis regions, which result in shorter travel distance for nonbleached fluorescent proteins, should demonstrate faster recoveries (Sprague *et al.*, 2004). Performing this experiment with IFT-A protein Ift122 we found that FRAP recovery kinetics were identical between the smaller and the larger bleaching regions, indicating that our recovery is in a binding-dominant regime (Figure 5E).

Having established a binding-dominant regime, we then utilized curve-fitting to quantify the off-rate for basal body binding (k_{off}) and the mobile fraction (A) (Sprague *et al.*, 2004). Fluorescence recovery as a function of time $f(t)$ was fit to the following equation: $f(t) = A\left(1 - e^{-k_{off}t}\right)$ and determined an off-rate of 0.045 s^{-1} (Figure 5, F and G).

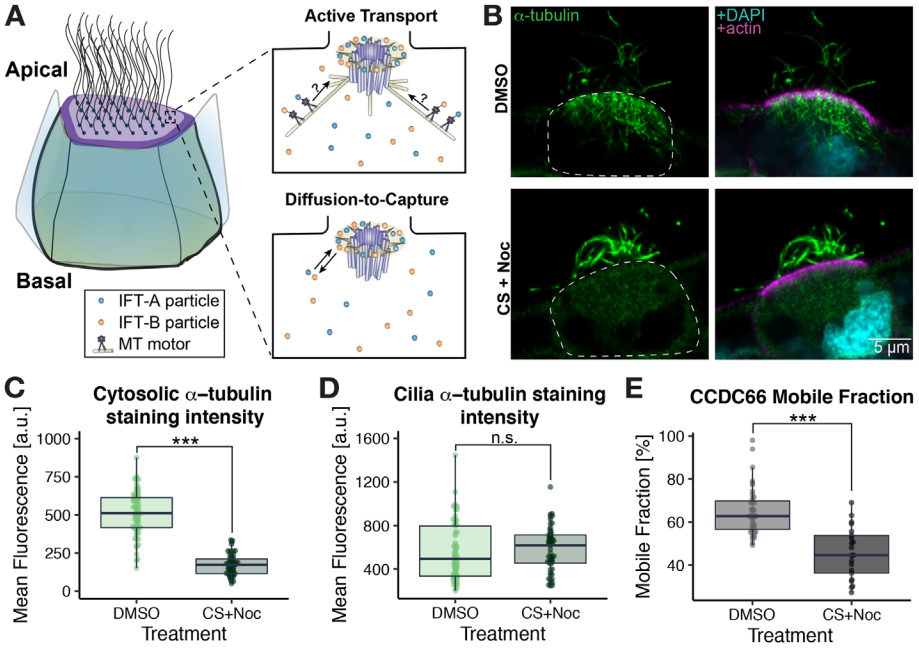

FIGURE 4: Cold-shock + nocodazole (CS + Noc) treatment eliminates cytosolic MTs and disrupts the dynamics of Ccdc66 at basal bodies. (A) Schematic representation of MCC depicting the two proposed mechanisms for IFT recruitment to basal bodies: active transport (top panel) and diffusion-to-capture (bottom panel). (B) Transverse sections of *Xenopus* MCCs stained for a-tubulin to verify efficacy of treatment. Actin (stained by Alexa Fluor 555 Phalloidin) and DAPI show the apical domain and nuclei, respectively. DMSO (mock)-treated cells are shown in the top panels and CS+Noc-treated cells in the bottom panels. (C) Cytosolic a-tubulin staining quantification for DMSO vs. CS+Noc-treated embryos. (D) Ciliary a-tubulin staining quantification for DMSO vs. CS+Noc-treated embryos. (E) Mobile fraction comparison of basal body turnover kinetics of Ccdc66 between DMSO and CS+Noc treatment.

Next, we sought to further characterize the kinetics of this diffusion-to-capture method by using a kinetic modeling approach (Phair and Misteli, 2001). We used a Monte Carlo model to simulate IFT particles moving on a lattice, with a diffusion coefficient *D* (Figure 5F). If these particles encountered the basal body, simulated by a capture site with a boundary of 400 × 400 nm, they displayed a probability of binding dependent on the pseudo-first-order rate constant for binding (k^*_{on}) (Sprague *et al.*, 2004). Molecules that were captured displayed a probability of unbinding dependent on the previously established $k_{off} = 0.045\ s^{-1}$. Using this method, we simulated the turnover FRAP experiments and determined that D = 1 $\mu m^2/s$ and $k^*_{on} = 0.5\ s^{-1}$ closely recapitulated experimental data for representative IFT-A protein GFP-Ift122 (Figure 5G). As expected for a protein of >100 kDa that is a member of a ~1 MDa complex, this diffusion coefficient is slower than cytosolic GFP (Potma *et al.*, 2001), but faster than mRNAs undergoing translation (Yan *et al.*, 2016). We expect the kinetic values obtained here for diffusion-to-capture will help further efforts to characterize IFT capture in the peri-basal body pool.

While it has become evident that the distal appendage matrix appears to be the docking site for IFT proteins in the peri-basal body pool (Deane *et al.*, 2001; Yang *et al.*, 2018), the specific capture mechanism is still unclear. In vitro reconstitution of the centrosome, which is a modified centriole like basal bodies, elucidated the molecular requirements for MT nucleation (Stearns and Kirschner, 1994; Woodruff *et al.*, 2017), and in vitro reconstitution was similarly essential for elucidating the architecture of the IFT-B complex (Taschner *et al.*, 2016). The quantification of in vivo rate constants presented here provides a useful foundation for future in vitro efforts to reconstitute IFT binding to the distal appendage matrix. Additionally, it will be interesting to further elucidate the changes to these rate constants using perturbations that affect the peri-basal body pool of IFT in previous, static assays (Singla *et al.*, 2010; Schmidt *et al.*, 2012; Čajánek and Nigg, 2014).

CONCLUSIONS

Elucidating the mechanisms of IFT proteins' dynamic localization from the cytoplasm to the peri-basal body pool and their retention there is a crucial challenge in understanding both ciliogenesis and cilia homeostasis. Here, we demonstrate a diffusion-to-capture mechanism governing IFT localization to basal bodies through quantification of IFT dynamics in vertebrate MCCs. Additionally, we show the recruitment of IFT proteins is dependent on their interaction partners. IFT-A and IFT-B, show independent recovery dynamics, suggesting that different protein–protein interactions facilitate the capture of IFT-A and IFT-B complexes at the basal body. This result is consistent with findings in *Chlamydomonas* that IFT-A and IFT-B proteins occupy unique domains in the peri-basal body pool (Hou *et al.*, 2007; Brown *et al.*, 2015).

Further characterization of basal body capture will help delineate which domains of the basal body correspond to the steps of IFT capture and train assembly. Presumably, IFT capture and train assembly are separate steps. Indeed, recruitment to the peri-basal body pool and train incorporation of IFT-A can be separated in mutants of Ift74 (Brown *et al.*, 2015). Additionally, while IFT-B is required for train formation, we show here that IFT-A protein Ift122 does not require IFT-B Ift52 for normal basal body turnover dynamics. Moving forward, it will be interesting to determine how peri-basal body capture mechanisms influence the assembly of IFT machinery into trains.

MATERIALS AND METHODS

Request a protocol through *Bio-protocol*.

Xenopus embryo manipulations

All experiments were conducted following animal ethics guidelines of the University of Texas at Austin, protocol number AUP-2018-00225. Female adult *X. laevis* were induced to ovulate by injection of human chorionic gonadotropin. The following day, females were squeezed, and eggs were fertilized in vitro with homogenized testis. Embryos were dejellied in 1/3× Marc's modified Ringer's (MMR) with 3% (wt/vol) cysteine (pH 7.9) at the two-cell stage. All embryos were reared in 1/3× MMR solution until the appropriate stage. For microinjections, embryos were placed in 2% Ficoll in 1/3× MMR and injected using a glass needle, forceps, and an Oxford universal micromanipulator.

Immunostaining

Immunostaining protocol was modified from Lee *et al.* (2008). Stage 27 *Xenopus* embryos were fixed using 1× MEMFA for 2 h on

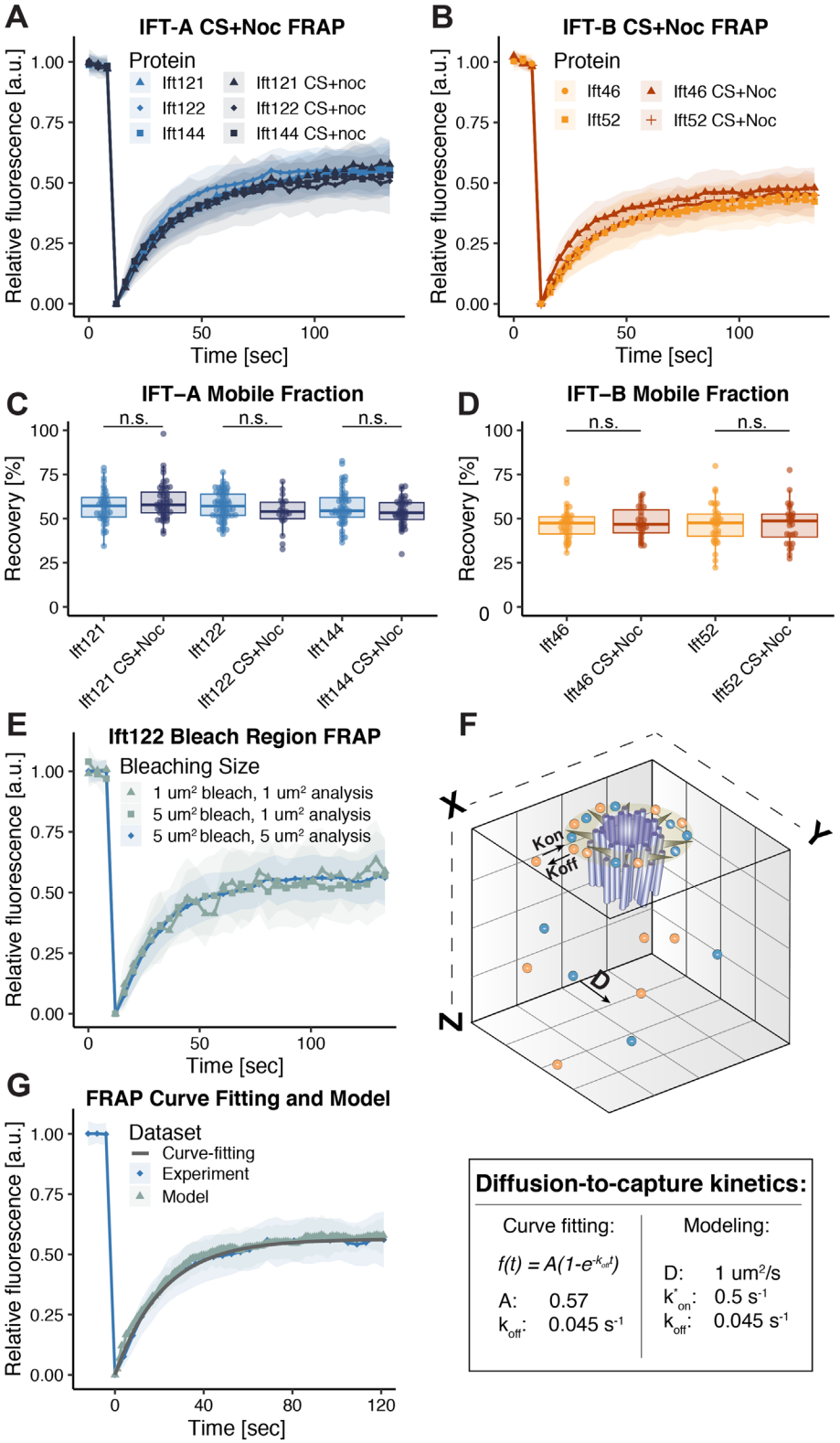

FIGURE 5: Cytosolic MTs are dispensable for IFT recruitment to basal bodies. (A) FRAP recovery curves of IFT-A proteins with and without CS+Noc treatment. (B) FRAP recovery curves of IFT-B proteins with and without CS+Noc treatment. (C) Mobile fraction comparison of basal body turnover kinetics of IFT-A proteins between no treatment and CS+Noc treatment. (D) Mobile fraction comparison of basal body turnover kinetics of IFT-B proteins between no treatment and CS+Noc treatment. (E) FRAP recovery curves of GFP-Ift122 with 5 and 1 μm² bleaching regions. (F) Schematic representation of diffusion-to-capture, with modeling parameters depicted. The table displays the equation used and parameters obtained. (G) Experimental and model FRAP recovery curves of GFP-Ift122, with the curve-fitting equation line overlaid.

a rotating mixer at room temperature immediately following either DMSO or cold-shock and nocodazole treatment. For transverse sections, embryos were embedded in 2% agarose, and thick (~250 μm) sections were cut using a Vibratome 1000 system. Sections were further fixed in 1× MEMFA for 1 h at room temperature.

Both whole-mount embryos and transverse sections were washed in TBST (155 mM NaCl, 10 mM Tris-Cl, 0.1% Triton X-100, pH 7.4) and blocked in 10% NGS, 5% DMSO in TBST. Monoclonal mouse anti-alpha-tubulin (DSHB, AA4.3, 1:200 dilution) was used as a primary antibody. Anti-alpha-tubulin was detected using Alexa Fluor 488 goat anti-mouse (Invitrogen, 1:1000). In addition, nuclei were stained using DAPI (1:1000) and actin was stained using Alexa Fluor 568 Phalloidin (Invitrogen, 1:500). Images were acquired on a Zeiss LSM700 laser scanning confocal microscope using a 100× oil objective lens.

Ciliary and cytosolic alpha-tubulin staining intensity quantification was performed by drawing a ROI around the ciliary or cytosolic regions of a single MCC and measuring the mean intensity of that region using Fiji (Schindelin *et al.*, 2012). For comparisons of alpha-tubulin intensity between DMSO- and CS+noc-treated embryos, a minimum of 55 cells from four embryos were quantified per condition.

Plasmids and cloning

Previously described vectors containing the following inserts were used: Ift43-GFP (Brooks and Wallingford, 2013), Ift121-GFP (Toriyama *et al.*, 2016), GFP-Ift122 (Toriyama *et al.*, 2016), Ift144-GFP (Toriyama *et al.*, 2016), Ift20-GFP (Brooks and Wallingford, 2012), Ift81-GFP (Toriyama *et al.*, 2016), GFP-Ofd1 (Toriyama *et al.*, 2016), Cep164-GFP (Toriyama *et al.*, 2016), GFP-Ttbk2 (Tu *et al.*, 2018), Centrin2-BFP (Tu *et al.*, 2018), and a-tub MAP7-RFP.

For new inserts, gene sequences were obtained from Xenbase (www.xenbase.org) (Karimi *et al.*, 2018). Open reading frames were amplified from a *Xenopus* cDNA library by polymerase chain reaction and then inserted into either a pCS10R or a pCS vector. All constructs were verified by sequencing.

mRNA, morpholino, and plasmid microinjections

Vectors were linearized by restriction digestion and capped mRNAs were synthesized using the mMESSAGE mMACHINE SP6 transcription kit (ThermoFisher Scientific, #AM1340).

For KD experiments, we used the previously described antisense morpholino oligonucleotides (MOs) against *Ift52*, 5′-AAGCAATC TGTTTGTTGACTCCCAT-3′ (GeneTools) (Dammermann *et al.*, 2009; Drew *et al.*, 2017).

Xenopus embryos were injected with mRNAs, plasmids, and/or MOs in the two ventral blastomeres at the four-cell stage to target the epidermis. mRNAs were injected at 70–200 pg per blastomere, Ift52 morpholino was injected at 40 ng per blastomere, and plasmids were injected at 25-75 pg per blastomere.

Live imaging, FRAP, and image analysis

For live imaging, *Xenopus* embryos (stage 26–29) were mounted between two coverslips and submerged in 0.3× MMR and imaged using a Nikon A1R scanning confocal microscope with a 60× oil immersion objective.

For FRAP experiments, a ROI of either 2.5 × 2.0 µm (all FRAP experiments unless otherwise stated) or 1 × 1 µm, focusing on the basal bodies of a MCC, was defined. Bleaching was performed on the ROI using 35% laser power of either a 405- or a 488-nm wavelength laser. Images of the bleached cell and a neighboring nonbleached MCC (which was used for subsequent bleach correction) were acquired. Bleach correction and FRAP curve-fitting was carried out using a custom Python script (modified from http://imagej.net/Analyze_FRAP_movies_with_a_Jython_script). For WT FRAP analysis of each IFT protein, a minimum of 35 cells from at least five independent embryos in three different clutches was analyzed. For complete numbers, see Supplemental Table S1.

The fluorescence intensity of Ift46-mNG at basal bodies was measured as previously described (Toriyama *et al.*, 2016). Briefly, basal bodies were determined using the three-dimensional (3D) object counter plugin of Fiji software, with the object size filter minimum set to 20 and the threshold set to the plugin's recommended value. At least 12 basal bodies per cell from at least 24 cells in three independent embryos were analyzed.

Cold shock and drug treatment

To depolymerize cytosolic MTs, a combination of cold shock and nocodazole treatment (CS + noc) was used. First, embryos were equilibrated in a solution of 25 µM nocodazole in 0.1× MMR for a minimum of 15 min. Cold-shock was performed by adding the embryos to 25 µM nocodazole in 0.1× MMR prechilled to 5°C for 15 min. Embryos were allowed to return to room temperature and maintained in 25 µM nocodazole in 0.1× MMR for imaging.

To ensure efficient and persistent depolymerization of MTs, treated embryos utilized for FRAP live imaging were co-injected with the MT binding domain ensconsin of MAP7 (α-tubulin MAP7-RFP). Nontreated embryos showed robust ensconsin labeling of cytosolic MTs, while CS+noc-treated embryos only showed ensconsin signal at basal bodies. For FRAP analysis of CS+noc-treated proteins, a minimum of 20 cells from four independent embryos was utilized.

Deciliation and ciliary regeneration

Deciliation was performed as previously described (Werner and Mitchell, 2013). Briefly, embryos were incubated in deciliation buffer (75 mM calcium, 0.02% NP40 in 0.1× MMR+antibiotic [50 µg/ml gentamicin]) at room temperature for 5 min. Embryos were washed in 0.1× MMR + antibiotic for 2 min, maintained in 1/3× MMR for specified periods of regeneration time, then mounted for imaging.

Cilia length was measured in Fiji (Schindelin *et al.*, 2012) from Z-stack images acquired of each timepoint. A segmented line was drawn along the length of each cilia with a clearly defined base and tip. Ciliary length was quantified from a minimum of 20 cells from at least two embryos per timepoint.

Additionally, FRAP was performed on embryos at different stages of cilia regeneration. A minimum of 25 cells was imaged from at least three embryos per timepoint.

Analysis of IFT binding kinetics from FRAP curve fitting

For verification of binding-dominant regime in FRAP experiments, the ROI was reduced from 5 to 1 μm^2 in experiments and analysis, or only when analyzing as indicated. For experiments and analysis, a ROI of 1 × 1 µm was bleached and this same area was measured as described above in postbleach image analysis. For analysis only, a 2.5 × 2.0 µm was still bleached. However, in postbleach image analysis, a ROI focusing on the center 1 × 1 µm of the 2.5 × 2.0 µm bleached region was measured.

Fluorescence recovery as a function of time was fit to the following equation: $f(t) = A\left(1 - e^{-k_{off}t}\right)$ utilizing custom nonlinear model fitting within MATLAB's curve fitting toolbox.

Monte Carlo model of diffusion-to-capture

Diffusion and binding in a 3D environment were modeled as a random walk process, with simulations run in MATLAB; 20 thousand randomly distributed particles move in a 2 × 2 × 4 µm cubic lattice with reflecting boundary conditions. If the molecules move within an apical capture radius of 400 × 400 nm, simulating the basal body, they have the probability of binding, dependent on their binding kinetics (k^*_{on}). Unbinding from the basal body is stochastic, but with a probability influenced by k_{off}.

To ensure proper simulation of diffusion in the model, the cubic lattice was expanded (to prevent confined diffusion), k^*_{on} and k_{off} were set to zero. In this scenario, we saw appropriate scaling of area explored, with $< \Delta x^2 (t) > = 6Dt$. Additionally, proper binding was determined by ensuring the number of molecules bound, *pBound*, scaled linearly with increases in k^*_{on}/k_{off}.

Statistical analysis and data visualization

Plots were generated using custom R scripts, utilizing the gglplot2 package (Wickham, 2016). One-way analysis of variance comparison of FRAP mobile fraction values between basal-body proteins and of ciliary length measurements during regeneration were carried out utilizing the afex R package (Singmann *et al.*, 2015). Differences between treated and nontreated mobile fraction values were analyzed using Welch's *t*-test. *P* values greater than 0.05 are reported as nonsignificant (n.s.), *0.05 > p > 0.005, **0.005 > p > 0.0005, and ***p < 0.005.

ACKNOWLEDGMENTS

The authors thank D. Dickinson, E. Roberson, and N. Stolpner for critical discussions and reading. Additionally, we thank the instructors and students in the Physical Biology of the Cell course at the Marine Biology Laboratory for inspiring more quantitative analysis of live imaging data. In particular, J.V.K.H. thanks course instructor Elena Koslover at University of California, San Diego for her support and advice on early iterations of the diffusion-to-capture model. Work in the JBW Lab was supported by the National Institute of Child Health and Human Development (R01HD085901) and the National Heart Lung-Blood Institute (R01HL117164). J.V.K.H. was supported by the Provost's Graduate Excellence Fellowship from the University of Texas at Austin (UT Austin), and N.V. was supported by the Dean's Strategic Fellowship from UT Austin. RS was supported by National Science Foundation grant CHE 1566001.

REFERENCES

Adler PN, Wallingford JB (2017). From planar cell polarity to ciliogenesis and back: the curious tale of the PPE and CPLANE proteins. Trends Cell Biol 27, 379–390.

Ahmed NT, Gao C, Lucker BF, Cole DG, Mitchell DR (2008). ODA16 aids axonemal outer row dynein assembly through an interaction with the intraflagellar transport machinery. J Cell Biol 183, 313–322.

Axelrod D, Koppel D, Schlessinger J, Elson E, Webb WW (1976). Mobility measurement by analysis of fluorescence photobleaching recovery kinetics. Biophys J 16, 1055.

Behal RH, Miller MS, Qin H, Lucker BF, Jones A, Cole DG (2012). Subunit interactions and organization of the Chlamydomonas reinhardtii intraflagellar transport complex A proteins. J Biol Chem 287, 11689–11703.

Behnke O, Forer A (1967). Evidence for four classes of microtubules in individual cells. J Cell Sci 2, 169–192.

Bhogaraju S, Cajanek L, Fort C, Blisnick T, Weber K, Taschner M, Mizuno N, Lamla S, Bastin P, Nigg EA, Lorentzen E (2013). Molecular basis of tubulin transport within the cilium by IFT74 and IFT81. Science (New York, NY) 341, 1009–1012.

Brooks ER, Wallingford JB (2012). Control of vertebrate intraflagellar transport by the planar cell polarity effector Fuz. J Cell Biol 198, 37–45.

Brooks ER, Wallingford JB (2013). The Small GTPase Rsg1 is important for the cytoplasmic localization and axonemal dynamics of intraflagellar transport proteins. Cilia 2, 13.

Brooks ER, Wallingford JB (2015). In vivo investigation of cilia structure and function using Xenopus. Methods Cell Biol 127, 131–159.

Brown JM, Cochran DA, Craige B, Kubo T, Witman GB (2015). Assembly of IFT trains at the ciliary base depends on IFT74. Curr Biol 25, 1583–1593.

Buisson J, Chenouard N, Lagache T, Blisnick T, Olivo-Marin JC, Bastin P (2013). Intraflagellar transport proteins cycle between the flagellum and its base. J Cell Sci 126, 327–338.

Burton PR (1968). Effects of various treatments on microtubules and axial units of lung-fluke spermatozoa. Z Zellforsch Mikrosk Anat 87, 226–248.

Čajánek L, Nigg EA (2014). Cep164 triggers ciliogenesis by recruiting Tau tubulin kinase 2 to the mother centriole. Proc Natl Acad Sci USA 111, E2841–E2850.

Cole DG, Diener DR, Himelblau AL, Beech PL, Fuster JC, Rosenbaum JL (1998). Chlamydomonas kinesin-II-dependent intraflagellar transport (IFT): IFT particles contain proteins required for ciliary assembly in Caenorhabditis elegans sensory neurons. J Cell Biol 141, 993–1008.

Conkar D, Bayraktar H, Firat-Karalar EN (2019). Centrosomal and ciliary targeting of CCDC66 requires cooperative action of centriolar satellites, microtubules and molecular motors. Scientific Rep 9, 1–17.

Conkar D, Culfa E, Odabasi E, Rauniyar N, Yates JR, Firat-Karalar EN (2017). The centriolar satellite protein CCDC66 interacts with CEP290 and functions in cilium formation and trafficking. J Cell Sci 130, 1450–1462.

Craft JM, Harris JA, Hyman S, Kner P, Lechtreck KF (2015). Tubulin transport by IFT is upregulated during ciliary growth by a cilium-autonomous mechanism. J Cell Biol 208, 223–237.

Dammermann A, Pemble H, Mitchell BJ, McLeod I, Yates JR, Kintner C, Desai AB, Oegema K (2009). The hydrolethalus syndrome protein HYLS-1 links core centriole structure to cilia formation. Genes Dev 23, 2046–2059.

De Brabander M, Van de Velre R, Aerts F, Borgers M, Janssen P (1976). The effects of methyl [5-(2-thienylcarbonyl)-1H-benzimidazol-2-yl] carbamate (R 17934; NSC 238159), a new synthetic antitumoral drug interfering with microtubules, on mammalian cells cultured in vitro. Cancer Res 36, 905–916.

Deane JA, Cole DG, Seeley ES, Diener DR, Rosenbaum JL (2001). Localization of intraflagellar transport protein IFT52 identifies basal body transitional fibers as the docking site for IFT particles. Curr Biol 11, 1586–1590.

Drew K, Lee C, Huizar RL, Tu F, Borgeson B, McWhite CD, Ma Y, Wallingford JB, Marcotte EM (2017). Integration of over 9,000 mass spectrometry experiments builds a global map of human protein complexes. Mol Syst Biol 13.

Engel BD, Ludington WB, Marshall WF (2009). Intraflagellar transport particle size scales inversely with flagellar length: revisiting the balance-point length control model. J Cell Biol 187, 81–89.

Fu W, Wang L, Kim S, Li J, Dynlacht BD (2016). Role for the IFT-A complex in selective transport to the primary cilium. Cell Rep 17, 1505–1517.

Goetz SC, Liem Jr KF, Anderson KV (2012). The spinocerebellar ataxia-associated gene Tau tubulin kinase 2 controls the initiation of ciliogenesis. Cell 151, 847–858.

Hao L, Thein M, Brust-Mascher I, Civelekoglu-Scholey G, Lu Y, Acar S, Prevo B, Shaham S, Scholey JM (2011). Intraflagellar transport delivers tubulin isotypes to sensory cilium middle and distal segments. Nat Cell Biol 13, 790.

Harris JA, Liu Y, Yang P, Kner P, Lechtreck KF (2016). Single-particle imaging reveals intraflagellar transport-independent transport and accumulation of EB1 in Chlamydomonas flagella. Mol Biol Cell 27, 295–307.

Hildebrandt F, Benzing T, Katsanis N (2011). Ciliopathies. New Engl J Med 364, 1533–1543.

Hoebeke J, Van Nijen G, De Brabander M (1976). Interaction of oncodazole (R 17934), a new antitumoral drug, with rat brain tubulin. Biochem Biophys Res Commun 69, 319–324.

Hou Y, Qin H, Follit JA, Pazour GJ, Rosenbaum JL, Witman GB (2007). Functional analysis of an individual IFT protein: IFT46 is required for transport of outer dynein arms into flagella. J Cell Biol 176, 653–665.

Jordan MA, Diener DR, Stepanek L, Pigino G (2018). The cryo-EM structure of intraflagellar transport trains reveals how dynein is inactivated to ensure unidirectional anterograde movement in cilia. Nat Cell Biol 20, 1250–1255.

Jurczyk A, Gromley A, Redick S, San Agustin J, Witman G, Pazour GJ, Peters DJ, Doxsey S (2004). Pericentrin forms a complex with intraflagellar transport proteins and polycystin-2 and is required for primary cilia assembly. J Cell Biol 166, 637–643.

Karimi K, Fortriede JD, Lotay VS, Burns KA, Wang DZ, Fisher ME, Pells TJ, James-Zorn C, Wang Y, Ponferrada VG (2018). Xenbase: a genomic, epigenomic and transcriptomic model organism database. Nucleic Acids Res 46, D861–D868.

Katoh Y, Terada M, Nishijima Y, Takei R, Nozaki S, Hamada H, Nakayama K (2016). Overall architecture of the intraflagellar transport (IFT)-B complex containing Cluap1/IFT38 as an essential component of the IFT-B peripheral subcomplex. J Biol Chem 291, 10962–10975.

Kozminski KG, Beech PL, Rosenbaum JL (1995). The Chlamydomonas kinesin-like protein FLA10 is involved in motility associated with the flagellar membrane. J Cell Biol 131, 1517–1527.

Kozminski KG, Johnson KA, Forscher P, Rosenbaum JL (1993). A motility in the eukaryotic flagellum unrelated to flagellar beating. Proc Natl Acad Sci USA 90, 5519–5523.

Lechtreck KF (2015). IFT-cargo interactions and protein transport in cilia. Trends Biochem Sci 40, 765–778.

LeDizet M, Piperno G (1986). Cytoplasmic microtubules containing acetylated alpha-tubulin in Chlamydomonas reinhardtii: spatial arrangement and properties. J Cell Biol 103, 13–22.

Lee C, Kieserman E, Gray RS, Park TJ, Wallingford J (2008). Whole-mount fluorescence immunocytochemistry on Xenopus embryos. Cold Spring Harbor Protocols 2008, pdb. prot4957.

Lucker BF, Behal RH, Qin H, Siron LC, Taggart WD, Rosenbaum JL, Cole DG (2005). Characterization of the intraflagellar transport complex B core direct interaction of the IFT81 and IFT74/72 subunits. J Biol Chem 280, 27688–27696.

Lucker BF, Miller MS, Dziedzic SA, Blackmarr PT, Cole DG (2010). Direct interactions of intraflagellar transport complex B proteins IFT88, IFT52, and IFT46. J Biol Chem 285, 21508–21518.

Ludington WB, Wemmer KA, Lechtreck KF, Witman GB, Marshall WF (2013). Avalanche-like behavior in ciliary import. Procee Nat Acad Sci 110, 3925–3930.

Lv B, Wan L, Taschner M, Cheng X, Lorentzen E, Huang K (2017). Intraflagellar transport protein IFT52 recruits IFT46 to the basal body and flagella. J Cell Sci.

McInally SG, Kondev J, Dawson SC (2019). Length-dependent disassembly maintains four different flagellar lengths in Giardia. eLife 8.

Mukhopadhyay S, Wen X, Chih B, Nelson CD, Lane WS, Scales SJ, Jackson PK (2010). TULP3 bridges the IFT-A complex and membrane phosphoinositides to promote trafficking of G protein-coupled receptors into primary cilia. Genes Dev 24, 2180–2193.

Paoletti A, Moudjou M, Paintrand M, Salisbury JL, Bornens M (1996). Most of centrin in animal cells is not centrosome-associated and centrosomal centrin is confined to the distal lumen of centrioles. J Cell Sci. 109 (Pt 13), 3089–3102.

Pazour GJ, Dickert BL, Witman GB (1999). The DHC1b (DHC2) isoform of cytoplasmic dynein is required for flagellar assembly. J Cell Biol 144, 473–481.

Pazour GJ, Wilkerson CG, Witman GB (1998). A dynein light chain is essential for the retrograde particle movement of intraflagellar transport (IFT). J Cell Biol 141, 979–992.

Phair RD, Misteli T (2001). Kinetic modelling approaches to in vivo imaging. Nat Rev Mol Cell Biol 2, 898–907.

Piperno G, Mead K (1997). Transport of a novel complex in the cytoplasmic matrix of Chlamydomonas flagella. Proc Natl Acad Sci USA 94, 4457–4462.
Porter ME, Bower R, Knott JA, Byrd P, Dentler W (1999). Cytoplasmic dynein heavy chain 1b is required for flagellar assembly in Chlamydomonas. Mol Biol Cell 10, 693–712.
Potma EO, de Boeij WP, Bosgraaf L, Roelofs J, van Haastert PJ, Wiersma DA (2001). Reduced protein diffusion rate by cytoskeleton in vegetative and polarized dictyostelium cells. Biophys J 81, 2010–2019.
Prosser SL, Pelletier L (2020). Centriolar satellite biogenesis and function in vertebrate cells. J Cell Sci 133.
Qin H, Diener DR, Geimer S, Cole DG, Rosenbaum JL (2004). Intraflagellar transport (IFT) cargo: IFT transports flagellar precursors to the tip and turnover products to the cell body. J Cell Biol 164, 255–266.
Reits EA, Neefjes JJ (2001). From fixed to FRAP: measuring protein mobility and activity in living cells. Nat Cell Biol 3, E145.
Richey EA, Qin H (2012). Dissecting the sequential assembly and localization of intraflagellar transport particle complex B in Chlamydomonas. PLoS One 7, e43118.
Rosenbaum JL, Child F (1967). Flagellar regeneration in protozoan flagellates. J Cell Biol 34, 345–364.
Rosenbaum JL, Moulder JE, Ringo DL (1969). Flagellar elongation and shortening in Chlamydomonas: the use of cycloheximide and colchicine to study the synthesis and assembly of flagellar proteins. J Cell Biol 41:600–619.
Sandoz D, Chailley B, Boisvieux-Ulrich E, Lemullois M, Laine MC, Bautista-Harris G (1988). Organization and functions of cytoskeleton in metazoan ciliated cells. Biol Cell 63, 183–193.
Schindelin J, Arganda-Carreras I, Frise E, Kaynig V, Longair M, Pietzsch T, Preibisch S, Rueden C, Saalfeld S, Schmid B, *et al*. (2012). Fiji: an open-source platform for biological-image analysis. Nat Methods 9, 676–682.
Schmidt KN, Kuhns S, Neuner A, Hub B, Zentgraf H, Pereira G (2012). Cep164 mediates vesicular docking to the mother centriole during early steps of ciliogenesis. J Cell Biol 199, 1083–1101.
Sigg MA, Menchen T, Lee C, Johnson J, Jungnickel MK, Choksi SP, Garcia G 3rd, Busengdal H, Dougherty GW, Pennekamp P (2017). Evolutionary proteomics uncovers ancient associations of cilia with signaling pathways. Dev Cell 43, 744–762.e711.
Signor D, Wedaman KP, Orozco JT, Dwyer ND, Bargmann CI, Rose LS, Scholey JM (1999). Role of a class DHC1b dynein in retrograde transport of IFT motors and IFT raft particles along cilia, but not dendrites, in chemosensory neurons of living Caenorhabditis elegans. J Cell Biol 147, 519–530.
Singla V, Romaguera-Ros M, Garcia-Verdugo JM, Reiter JF (2010). Ofd1, a human disease gene, regulates the length and distal structure of centrioles. Dev Cell 18, 410–424.
Singmann H, Bolker B, Westfall J, Aust F (2015). afex: Analysis of factorial experiments. R package version 0.13–145.
Sprague BL, McNally JG (2005). FRAP analysis of binding: proper and fitting. Trends Cell Biol 15, 84–91.
Sprague BL, Pego RL, Stavreva DA, McNally JG (2004). Analysis of binding reactions by fluorescence recovery after photobleaching. Biophys J 86, 3473–3495.
Stearns T, Kirschner M (1994). In vitro reconstitution of centrosome assembly and function: the central role of γ-tubulin. Cell 76, 623–637.
Sung C-H, Leroux MR (2013). The roles of evolutionarily conserved functional modules in cilia-related trafficking. Nat Cell Biol 15, 1387–1397.
Tai AW, Chuang JZ, Bode C, Wolfrum U, Sung CH (1999). Rhodopsin's carboxy-terminal cytoplasmic tail acts as a membrane receptor for cytoplasmic dynein by binding to the dynein light chain Tctex-1. Cell 97, 877–887.
Tamm SL (1967). Flagellar development in the protozoan Peranema trichophorum. J Experimental Zool 164, 163–186.
Taschner M, Bhogaraju S, Vetter M, Morawetz M, Lorentzen E (2011). Biochemical mapping of interactions within the intraflagellar transport (IFT) B core complex IFT52 binds directly to four other IFT-B subunits. J Biol Chem 286, 26344–26352.
Taschner M, Kotsis F, Braeuer P, Kuehn EW, Lorentzen E (2014). Crystal structures of IFT70/52 and IFT52/46 provide insight into intraflagellar transport B core complex assembly. J Cell Biol 207, 269–282.
Taschner M, Lorentzen E (2016). The Intraflagellar Transport Machinery. Cold Spring Harb Perspect Biol 8.
Taschner M, Weber K, Mourao A, Vetter M, Awasthi M, Stiegler M, Bhogaraju S, Lorentzen E (2016). Intraflagellar transport proteins 172, 80, 57, 54, 38, and 20 form a stable tubulin-binding IFT-B2 complex. EMBO J 35, 773–790.
Toriyama M, Lee C, Taylor SP, Duran I, Cohn DH, Bruel AL, Tabler JM, Drew K, Kelly MR, Kim S, *et al*. (2016). The ciliopathy-associated CPLANE proteins direct basal body recruitment of intraflagellar transport machinery. Nat Genet 48, 648–656.
Tu F, Sedzinski J, Ma Y, Marcotte EM, Wallingford JB (2018). Protein localization screening in vivo reveals novel regulators of multiciliated cell development and function. J Cell Sci 131, jcs206565.
Tucker JB (1984). Spatial organization of microtubule-organizing centers and microtubules. J Cell Biol 99, 55s–62s.
Vashishtha M, Walther Z, Hall JL (1996). The kinesin-homologous protein encoded by the Chlamydomonas FLA10 gene is associated with basal bodies and centrioles. J Cell Sci 109 (Pt 3), 541–549.
Walentek P, Quigley IK (2017). What we can learn from a tadpole about ciliopathies and airway diseases: Using systems biology in Xenopus to study cilia and mucociliary epithelia. Genesis 55, e23001.
Walther Z, Vashishtha M, Hall JL (1994). The Chlamydomonas FLA10 gene encodes a novel kinesin-homologous protein. J Cell Biol 126, 175–188.
Webb S, Mukhopadhyay AG, Roberts AJ (2020). Intraflagellar transport trains and motors: Insights from structure. Semin Cell Dev Biol 107, 82–90.
Werner ME, Mitchell BJ (2012). Understanding ciliated epithelia: the power of Xenopus. Genesis 50, 176–185.
Werner ME, Mitchell BJ (2013). Using Xenopus skin to study cilia development and function. Methods Enzymol 525, 191–217.
Wickham H (2016). ggplot2: elegant graphics for data analysis. Springer.
Wingfield JL, Mengoni I, Bomberger H, Jiang YY, Walsh JD, Brown JM, Picariello T, Cochran DA, Zhu B, Pan J, *et al*. (2017). IFT trains in different stages of assembly queue at the ciliary base for consecutive release into the cilium. eLife 6.
Woodruff JB, Gomes BF, Widlund PO, Mahamid J, Honigmann A, Hyman AA (2017). The centrosome is a selective condensate that nucleates microtubules by concentrating tubulin. Cell 169, 1066–1077.e1010.
Wren KN, Craft JM, Tritschler D, Schauer A, Patel DK, Smith EF, Porter ME, Kner P, Lechtreck KF (2013). A differential cargo-loading model of ciliary length regulation by IFT. Curr Biol 23, 2463–2471.
Yan X, Hoek TA, Vale RD, Tanenbaum ME (2016). Dynamics of translation of single mRNA molecules in vivo. Cell 165, 976–989.
Yang TT, Chong WM, Wang W-J, Mazo G, Tanos B, Chen Z, Tran TMN, Chen Y-D, Weng RR, Huang C-E (2018). Super-resolution architecture of mammalian centriole distal appendages reveals distinct blade and matrix functional components. Nat Commun 9, 2023.
Yang TT, Tran MNT, Chong WM, Huang CE, Liao JC (2019). Single-particle tracking localization microscopy reveals nonaxonemal dynamics of intraflagellar transport proteins at the base of mammalian primary cilia. Mol Biol Cell 30, 828–837.
Zhu B, Zhu X, Wang L, Liang Y, Feng Q, Pan J (2017). Functional exploration of the IFT-A complex in intraflagellar transport and ciliogenesis. PLoS Genet 13, e1006627.